nature communications

Article

https://doi.org/10.1038/s41467-024-50979-6

Efficient photoredox catalysis in C–C cross-coupling reactions by two-coordinated Au(I) complex

Received: 16 February 2024

Accepted: 26 July 2024

Published online: 03 August 2024

Check for updates

Byung Hak Jhun[1], Jihoon Jang[2], Shinae Lee[1], Eun Jin Cho[2] ✉ & Youngmin You[1] ✉

Photocatalysis provides a versatile approach to redox activation of various organic substrates for synthetic applications. To broaden the scope of photoredox catalysis, developing catalysts with strong oxidizing or reducing power in the excited state is imperative. Catalysts that feature highly cathodic oxidation potentials and long lifetimes in their excited states are particularly in demand. In this research, we demonstrate the catalytic utility of two-coordinate Au(I) complex photocatalysts that exhibit an exclusive ligand-to-ligand charge-transfer (LLCT) transition in C–C cross-coupling reactions between *N*-heterocycles and (hetero)aryl halides, including redox-resistant (hetero)aryl chlorides. Our photocatalysis system can steer reactions under visible-light irradiation at a catalyst loading as low as 0.1 mol% and exhibits a broad substrate scope with high chemo- and regioselectivity. Our mechanistic investigations provide direct spectroscopic evidence for each step in the catalysis cycle and demonstrate that the LLCT-active Au(I) complex catalysts offer several benefits, including strong visible-light absorption, a 210 ns-long excited-state lifetime without short-lived components, and a 91% yield in the production of free-radical intermediates. Given the wide structural versatility of the proposed catalysts, we envision that our research will provide useful insights into the future utilization of the LLCT-active Au(I) complex for organic transformations.

Visible-light-activatable, homogeneous photoredox catalysis has emerged as a useful tool for a range of organic transformations[1,2]. The synthetic utility benefits from the ability of catalysts to generate free-radical intermediates through heterobimolecular photoinduced electron transfer[3]. To expand the synthetic utility, researchers have devoted considerable efforts to identifying catalyst molecules capable of mediating photoredox reactions[4]. Coordinatively saturated complexes with d^6 metals, such as *fac*-Ir(ppy)$_3$ (ppy = 2-phenylpyridinato) and [Ru(bpy)$_3$]$^{2+}$ (bpy = 2,2′-bipyridyl), constitute a family of successful molecular photoredox catalysts[2,5]. Their catalytic efficiencies benefit from the tunable, redox-active triplet metal-to-ligand charge-transfer (^{3}MLCT) transition state[2]. The ^{3}MLCT-active metal complexes, however, sometimes exhibit insufficient catalytic performance, especially for activating substrates with redox-resistant bonds, such as the C–Cl bond[6]. This limitation stems from detrimental effects of the central metal, including (1) an unavoidable energy loss in intersystem crossing from the initially photoexcited singlet state to the ^{3}MLCT transition state, (2) the occurrence of a metal-centered nonradiative process[7], and (3) the presence of electron-deficient metal centers, such as Ir(III), which are sometimes disadvantageous for achieving strong excited-state reducing power.

[1]Department of Chemical and Biomolecular Engineering, Yonsei University, Seoul 03722, Republic of Korea. [2]Department of Chemistry, Chung-Ang University, Seoul 06974, Republic of Korea. ✉e-mail: ejcho@cau.ac.kr; odds2@yonsei.ac.kr

We envisioned that low-valent metal complexes that avoid metal-involved electronic transitions could be promising candidates for overcoming the limitations of the ^{3}MLCT-active photoredox catalysts. To investigate this idea, we selected two-coordinated d^{10} Au(I) complexes with charge-neutral carbene and monoanionic amido ligands (Fig. 1). This heteroleptic structure exhibits strong visible-light absorption owing to the amido ligand-to-carbene ligand charge-transfer (LLCT) transition through redox-innocent mediation of the two mutually orthogonal Au 5*d* orbitals[8,9]. The singlet and triplet LLCT transition states are near-degenerate and in a rapid equilibrium due to strong spin–orbit coupling provided by the Au(I) center, effectively alleviating energy loss in the photocatalyst, which is substantial for

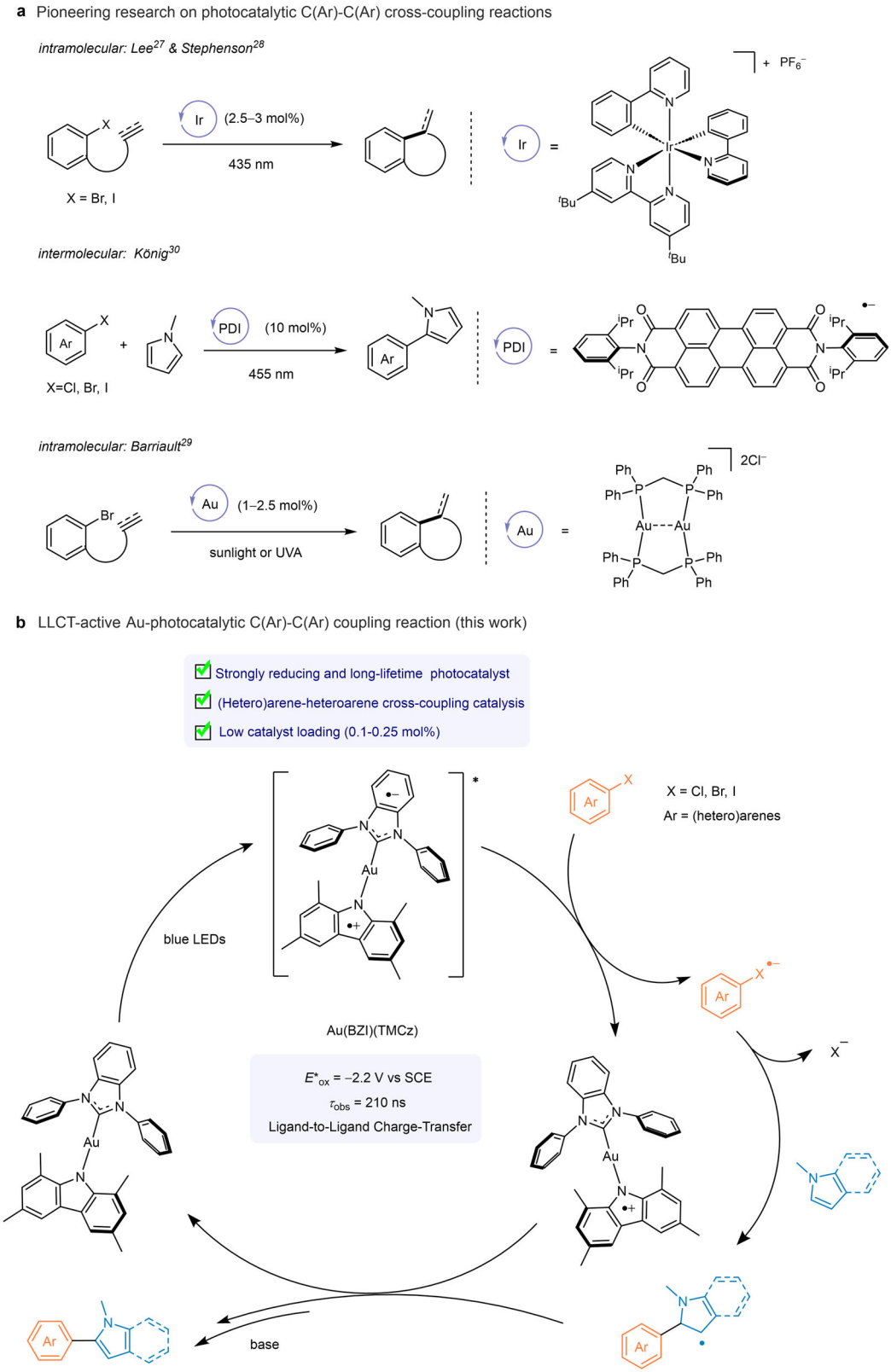

Fig. 1 | Photoredox catalytic C(Ar)–C(Ar) cross-coupling reactions. a, b Previous (**a**) and our (**b**) methods for photocatalytic C(Ar)–C(Ar) cross-coupling reactions.

https://doi.org/10.1038/s41467-024-50979-6

Table 1 | Photocatalyst screening for C–C cross-coupling reactions[a,b]

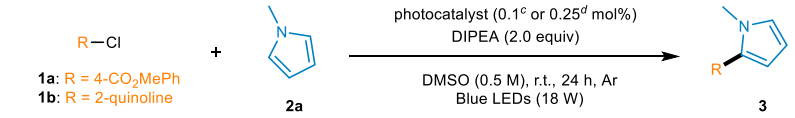

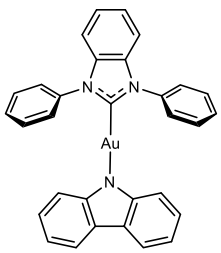

Au(BZI)(Cz)
3aa: 86%
3ba: 71%

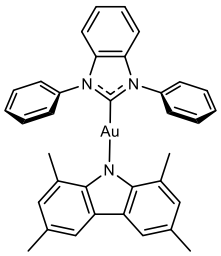

Au(BZI)(TMCz)
3aa: 91%
3ba: 84%

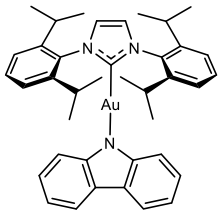

Au(IPr)(Cz)
3aa: 67% (22%)
3ba: 35% (49%)

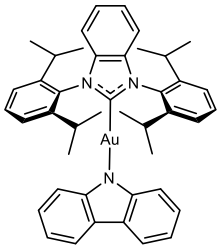

Au(^{Dipp}BZI)(Cz)
3aa: 39% (55%)
3ba: 33% (51%)

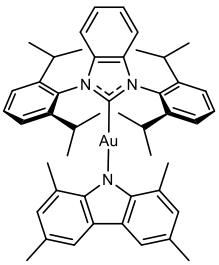

Au(^{Dipp}BZI)(TMCz)
3aa: 48% (47%)
3ba: 42% (36%)

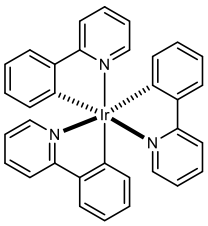

fac-Ir(ppy)$_3$
3aa: 65%
3ba: 8% (82%)

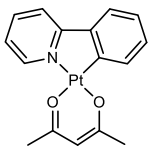

Ptppy: No reaction

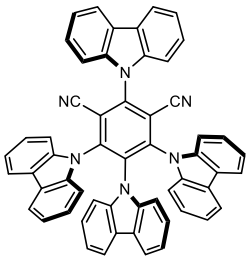

4CzIPN: No reaction

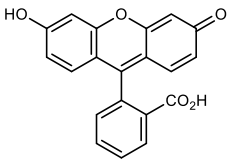

Fluorescein: No reaction

[a]Reaction scale: **1** (0.05 mmol) and **2** (0.5 mmol).
[b]The yield was determined by ^{1}H NMR spectroscopy using bromoform as an internal standard, and values in parentheses are the percentage of the unreacted **1a**.
[c]With **1b**.
[d]With **1a**.

^{3}MLCT-active Ir(III) and Ru(II) photocatalysts[10,11]. Note that the Au center is hardly involved in redox processes in LLCT-active Au(I) complexes, which enables facile control of the excited-state oxidation (E^*_{ox}) and reduction (E^*_{red}) potentials. In addition, the LLCT-active Au(I) complexes exhibit an excited-state lifetime (τ_{obs}) as long as several microseconds[12–14], without substantial contaminations by short-lived components; such contaminations are routinely observed for organic thermally activated delayed fluorescence (TADF) molecules, such as 1,2,3,5-tetrakis(carbazol-9-yl)-4,6-dicyanobenzene (4CzIPN) shown in Table 1[15]. We thus speculate that (1) the negligible electronic energy loss, (2) the absence of metal-centered valence change, (3) the less-electron-deficient Au(I) center, and (4) the efficient utilization of the long-lived excited state will make LLCT-active Au(I) complexes potent photoreducing catalysts.

Previous research on photocatalytic Au complexes has mainly focused on the identification of metal-centered redox behaviors. For example, a dinuclear Au(I) complex with bisphosphino bridging ligands exhibited an E^*_{ox} value as negative as −1.6 V vs a NaCl-saturated calomel electrode because of the Au(I/II) redox cycle (Fig. 1a)[16,17]. The two-electron cycle between Au(I) and Au(III) species has also garnered research interest because it complies with the well-established oxidative addition–reductive elimination catalytic steps[18–20]. These groundbreaking advances promise the synthetic potential of Au(I) complexes, although their catalytic utility is still based on the metal-centered redox processes involving Au(II) or Au(III), analogous to the case of ^{3}MLCT-active complexes. The photocatalysis ability of LLCT-active Au(I) complexes was recently validated for [2 + 2] cycloaddition[21] and water reduction reactions[22]. The catalysis involved energy transfer and the reductive formation of metal nanoparticles, respectively, as the key processes. To the best of our knowledge, organic transformations driven by LLCT-active Au(I) complex photoredox catalysts remain unexplored.

Photocatalytic C–C bond formation plays a critical role in chemistry, driving molecular diversity and facilitating the synthesis of complex functional molecules, as briefly outlined in Fig. 1a[23–26]. The pioneering work conducted independently by the Lee[27] and Stephenson[28] groups on the intramolecular C–C bond formation of aryl iodides and bromides with π-substrates marked important advances. Despite under ultraviolet (UV) A irradiation, the MLCT-active dinuclear Au complex was also employed by the Barriault group for an intramolecular C–C coupling process[29]. Following these contributions, the scope of research has been significantly expanded to include intermolecular processes with a broader spectrum of substrates, particularly the more challenging aryl chloride substrates. This expansion has been based on strongly photoreducing catalysts such as the photoexcited doublet species utilized by Ghosh and coworkers[30]. Despite recent advances[31–35], a persistent need exists to develop more efficient and selective photocatalytic systems capable of activating redox-resistant substrates, such as aryl chlorides, for C–C cross-coupling reactions.

https://doi.org/10.1038/s41467-024-50979-6

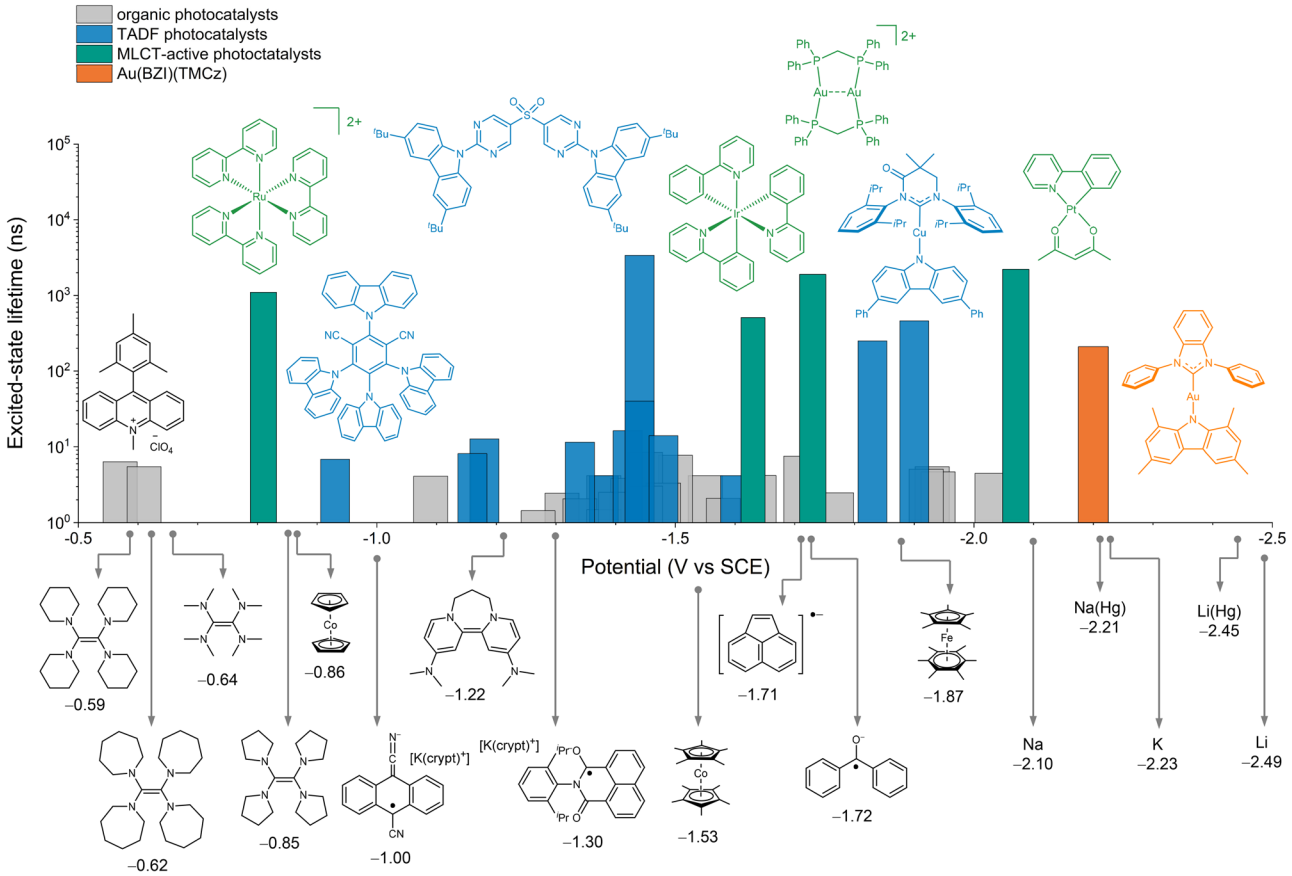

Fig. 2 | Photoreducing ability. Comparisons of excited-state lifetime and excited-state oxidation potentials of representative photocatalysts and Au(BZI)(TMCz). Shown at the bottom are chemical reducing agents. Refer to Supplementary Tables 1 and 2 for the values.

Herein, we report the strong photoredox catalytic reactivity and the corresponding mechanism of LLCT-active Au(I) complexes for C–C cross-coupling reactions (Fig. 1b). Au(BZI)(TMCz) (BZI = 1,3-diphenylbenzo[*d*]imidazolylidene; TMCz = 1,3,6,8-tetramethylcarbazolide) exhibited an E^*_{ox} value as negative as −2.16 V vs saturated calomel electrode (SCE), demonstrating the high reducing power close to sodium mercury amalgam (−2.21 V vs SCE) and metallic potassium (−2.23 V vs SCE). The E^*_{ox} value positions the Au(I) complex among the most potent photoreductants reported to date, underscoring its exceptional photoredox ability (see Fig. 2 and Supplementary Tables 1, 2). Our catalytic system features notable advantages, including a catalyst loading as low as 0.1 mol%, the reaction yields greater than 80%, and a broad substrate scope, including heteroaryl chlorides that are difficult to activate. Our mechanistic investigations based on steady-state and transient electronic spectroscopy, spectroelectrochemistry, and quantum chemical calculations revealed that the Au(I) complex photocatalyst exhibits strong photoreducing power, with the ability to efficiently retard charge recombination, characterized by a 91% efficiency for the reductive generation of a key radical intermediate from an aryl chloride. In addition, our spectroscopic studies identified the neutralization of the one-electron-oxidized catalyst as the rate-determining step in the overall photoredox catalysis cycle.

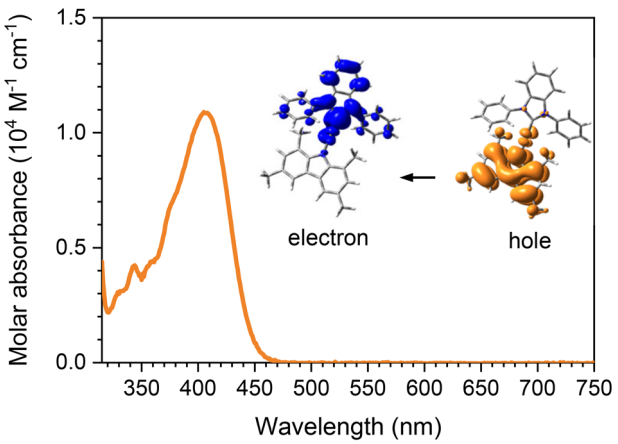

Fig. 3 | Photon absorption. UV–Vis absorption spectrum of Au(BZI)(TMCz) recorded in toluene at 298 K. Inset figures denote the hole and electron distributions calculated at the CAM-B3LYP level of theory for the singlet transition of the triplet geometry of Au(BZI)(TMCz) with exclusive ligand-to-ligand charge-transfer (LLCT) transition character. The LANL2DZ and 6–311+G(d) basis sets were used for the Au atom and the other atoms, respectively.

Results

Photocatalytic C–C cross-coupling reactions

A series of two-coordinated Au(I) complexes having *N*-heterocyclic carbene and carbazolide ligands with various alkyl substituents were selected as potent candidates for the visible light-absorbing photoredox catalysts. These complexes exhibit visible absorption due to the LLCT transition (Fig. 3 and Supplementary Fig. 1). For example, the ultraviolet–visible (UV–Vis) absorption spectrum of Au(BZI)(TMCz) has an onset wavelength of 470 nm (Fig. 3 and Supplementary Table 3). The excited state of Au(BZI)(TMCz) is long-lived, with a τ_{obs} as long as 210 ns in deaerated toluene, without any short-lived components (Supplementary Fig. 2). Au(BZI)(TMCz) exhibits ground-state

https://doi.org/10.1038/s41467-024-50979-6

Table 2 | Substrate scope[a,b]

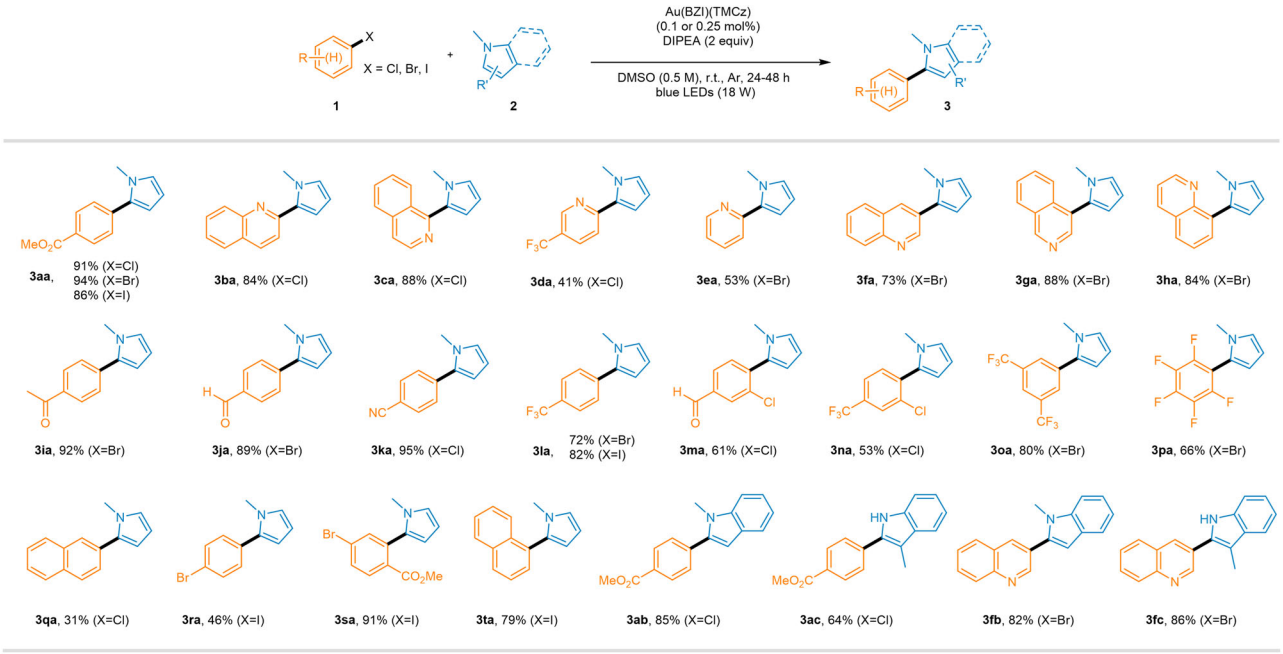

[a]Reaction scale: **1** (0.5 mmol) and **2** (5.0 mmol).
[b]Isolated yields, except ^{1}H NMR yields for **3da** and **3ea**, due to purification challenges from the protodebrominated products.

oxidation (E_{ox}) and reduction (E_{red}) potentials of 0.56 and −2.26 V vs SCE, respectively (Supplementary Fig. 3). The corresponding E^*_{ox} value is calculated to be −2.16 V vs SCE, being more cathodic than those of widely used photoredox catalysts such as Ptppy (−2.07 V vs SCE)[36], *fac*-Ir(ppy)$_3$ (−1.73 V vs SCE)[37], 4CzIPN (−1.18 V vs SCE)[4], and Mes−Acr$^+$ (−0.57 V vs SCE)[38]. It should be emphasized that, as compared in Fig. 2, Au(BZI)(TMCz) exhibits a balance between τ_{obs} and E^*_{ox}, which is a prerequisite for a potent photoreducing catalyst.

The photoredox catalytic efficacy of these Au(I) complexes was evaluated through comparisons with several established photoredox catalysts for an intermolecular C−C cross-coupling reaction between model (hetero)aryl chlorides (specifically, methyl-4-chlorobenzoate (**1a**) and 2-chloroquinoline (**1b**)) and *N*-methylpyrrole (**2a**) (Table 1). The reactions were carried out with a 0.25 mol% or a 0.1 mol% photocatalyst for **1a** or **1b**, respectively, and 2 equivalents of *N*,*N*-di(isopropyl)ethylamine (DIPEA) in Ar-saturated dimethyl sulfoxide (DMSO, 0.50 M) under blue LEDs (405 nm) irradiation. Notably, Au complexes without alkyl substituents in the carbene ligands, Au(BZI)(Cz) (Cz = carbazolide) and Au(BZI)(TMCz), exhibited superior reactivity, successfully yielding the desired C−C cross-coupled product **3** in 71–91% yields. The distinctly superior catalytic performance of Au(BZI)(Cz) and Au(BZI)(TMCz) compared with that of the other Au(I) complexes is attributable to their interactions with **2a**, being less sterically encumbered. The added **2a** results in an increase in τ_{obs}, suggesting that **2a** is not engaged in photoinduced electron transfer but suppresses nonradiative relaxation of the Au(I) complexes (Supplementary Fig. 2).

By contrast, the commonly used *fac*-Ir(ppy)$_3$ demonstrated lower reactivity, and 4CzIPN, fluorescein, and Ptppy[36] were inactive in this transformation. Optimization of the reaction parameters enabled the synthesis of the heteroaryl−heteroaryl coupled product (**3ba**) in 84% yield in the presence of only 0.1 mol% Au(BZI)(TMCz). The optimization results are compiled in Supplementary Table 4. Notably, this catalytic loading represents a significant advance, rearely reported in the literature. The quantum yield for the reaction of **1a** with **2a**, which was determined using the standard ferrioxalate actinometry, is as large as 34%. Finally, control experiments revealed that the reaction requires both the photocatalyst and irradiation with visible light (Supplementary Table 4).

With the reaction parameters in hand, we explored the versatility of the Au(I) complex-catalyzed C−C coupling protocol in synthesizing various (hetero)aryl− heteroaryl products (**3**). Au(BZI)(TMCz), which has an E^*_{ox} as negative as −2.16 V vs SCE, enables the incorporation of a range of redox-resistant (hetero)aryl chlorides (**1a**, **1b**, **1c**, **1k**, **1m**, **1n**, and **1q**) with reduction potentials (E_{red}s) in the range −1.61 to −2.12 V vs SCE (see Supplementary Fig. 4 for the corresponding voltammograms), as well as bromides and iodides, in the C−C coupled products (Table 2). We observed a distinct variation in the reactivity among different (hetero)aryl halides, leading to a chemoselective process. Specifically, in the case of dihalogenated substrates **1r** and **1s**, the iodo group demonstrated selective reactivity over the bromo substituent, resulting in **3ra** and **3sa** as the major products, respectively. For **1m** and **1n**, which contain two chloro substituents, regioselective reactivity was noted at the chloride positioned para to the aldehyde and CF_3 groups, yielding **3ma** and **3na**, respectively. In general, *N*-heteroaryl halides exhibited higher reactivities than aryl halides, even with a reduced catalyst loading (0.1 mol% vs 0.25 mol%). Furthermore, the substitution patterns did not affect reactivity: *ortho*-, *meta*-, and *para*-substituted aryl halides were all suitable. Notably, our photoredox catalysis protocol tolerated the presence of various functional groups, including aldehyde (**3ja** and **3ma**), ketone (**3ia**), ester (**3aa**, **3sa**, **3ab**, and **3ac**), and nitrile (**3ka**) groups, as well as medicinally significant fluoride (**3pa**) and CF_3 (**3da**, **3la**, **3na**, **3oa**) groups. In general, dehalogenation side products were also observed, albeit in negligible amounts (<5%) for bromide and iodide substrates.

Mechanistic investigations

Having demonstrated the photoredox catalytic ability of the Au(I) complex, we sought to elucidate the role of the catalyst in the C−C cross-coupling reaction. The E^*_{ox} value of Au(BZI)(TMCz) (−2.16 V vs SCE) is more negative than the E_{red} value of **1a** (−1.81 V vs SCE), implying that the excited state of Au(BZI)(TMCz) (denoted as

https://doi.org/10.1038/s41467-024-50979-6

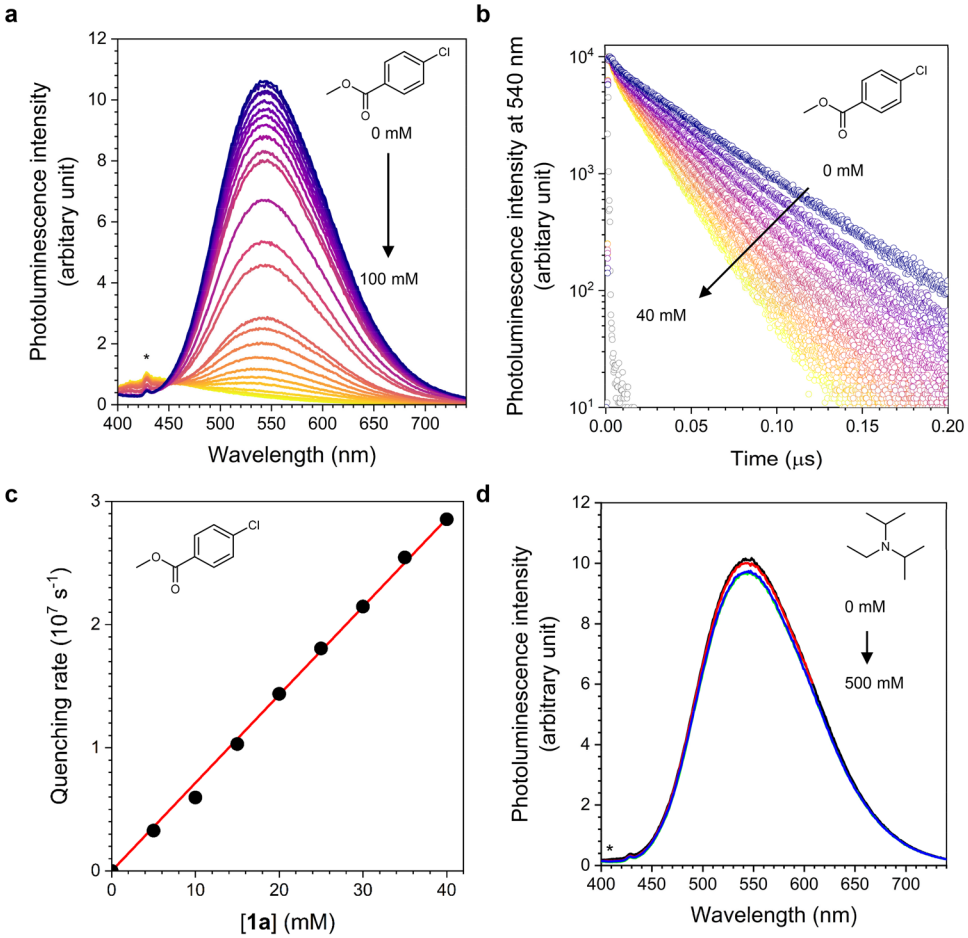

Fig. 4 | Oxidative quenching. a Photoluminescence (λ_{ex} = 380 nm) spectra of Ar-saturated DMSO containing 50 μM Au(BZI)(TMCz), recorded with increasing concentration of **1a** (0–100 mM). The peak marked with an asterisk (*) is the Raman signal of the solvent. **b** Photoluminescence decay traces of Ar-saturated DMSO containing 50 μM Au(BZI)(TMCz), recorded with increasing concentration of **1a** (0–40 mM) at a wavelength of 540 nm after picosecond pulsed laser photoexcitation at 377 nm (pulse duration = 25 ps). **c** Corresponding pseudo-first-order kinetics analysis of the quenching rate as a function of added **1a**. The quenching rate was calculated according to the relationship rate = $1/\tau_{obs}$(**1a**) − $1/\tau_{obs}$(0), where τ_{obs}(**1a**) and τ_{obs}(0) are the observed photoluminescence lifetime of 50 μM Au(BZI)(TMCz) in the presence and absence, respectively, of **1a**. **d** Photoluminescence (λ_{ex} = 380 nm) spectra of Ar-saturated DMSO containing 50 μM Au(BZI)(TMCz) recorded with increasing concentration of DIPEA (0–500 mM).

[Au(BZI)(TMCz)]* hereafter) can be oxidatively quenched by **1a** with the driving force for heterobimolecular one-electron transfer ($-\Delta G_{eT}$, $-\Delta G_{eT} = e\cdot[E^*_{ox}(\text{Au(BZI)(TMCz)}) - E_{red}(\textbf{1a})]$, where e is the elementary charge and we ignore the Coulomb term because of our use of the polar solvent DMSO of 0.35 eV). By contrast, reductive quenching of [Au(BZI)(TMCz)]* (E^*_{red} = 0.46 V vs SCE) by DIPEA (E_{ox} = 0.64 V vs SCE) is predicted to be disfavored due to the negative $-\Delta G_{eT}$ of −0.18 eV.

We validated the aforementioned thermodynamic considerations for the initial electron transfer by using photoluminescence titration experiments. As shown in Fig. 4a, the increased concentrations of **1a** (0–100 mM) elicit a concentration-dependent decrease in the photoluminescence intensity of 50 μM Au(BZI)(TMCz). An analogous decrease is also observed for τ_{obs} (Fig. 4b). The quenching rate computed through the relationship, quenching rate = $1/\tau_{obs}$(**1a**) − $1/\tau_{obs}$(0), where τ_{obs}(**1a**) and τ_{obs}(0) are the τ_{obs} of Au(BZI)(TMCz) in the presence and absence of **1a**, respectively, increases with the concentration of **1a** (Fig. 4c). In all cases, the decays of photoluminescence intensities obey the first-order kinetics to 19–45 ns. A plot of the pseudo-first-order quenching rate as a function of the concentration of **1a** is linear, with an apparent heterobimolecular quenching rate constant (k_q) of $7.2 \pm 0.1 \times 10^8\,M^{-1}\,s^{-1}$. Our Stern–Volmer analysis for the steady-state photoluminescence intensity data yields a similar k_q of $8.4 \pm 0.3 \times 10^8\,M^{-1}\,s^{-1}$ (Supplementary Fig. 5). Deconvolution of the diffusion rate constant (k_{diff}, $3.3 \times 10^9\,M^{-1}\,s^{-1}$ for DMSO at 298 K) from k_q yields a second-order quenching rate constant (k_Q) of $9.1 \pm 0.1 \times 10^8\,M^{-1}\,s^{-1}$. The quantum yield for quenching (Φ_Q) is as large as 95% in the presence of 0.50 M **1a**, which is estimated according to the relationship $\Phi_Q = k_Q\cdot[\textbf{1a}] / (k_Q\cdot[\textbf{1a}] + k_d)$, where [**1a**] is expressed in molarity (0.50 M) and k_d is the intrinsic decay rate of [Au(BZI)(TMCz)]* ($2.2 \times 10^7\,s^{-1}$). In stark contrast, DIPEA does not quench the photoluminescence of [Au(BZI)(TMCz)]* even at a concentration as high as 500 mM (Fig. 4d). The rapid deactivation of [Au(BZI)(TMCz)]* by **1a** can be ascribed to electron or energy transfer. We exclude the energy-transfer pathway because Au(BZI)(TMCz) not only exhibits negligible spectral overlap with **1a**, **2a**, and DIPEA but also exhibits a T_1 energy (2.79 eV) lower than that of **1a** (3.16 eV) (refer to Supplementary Fig. 6 for details). Collectively, our electrochemical and photoluminescence results strongly suggest rapid and exclusive electron transfer from [Au(BZI)(TMCz)]* to **1a**. Nanosecond laser flash photolysis investigations provide direct spectroscopic evidence for electron transfer (*vide infra*).

The photoinduced electron transfer produces a radical-ion pair (RIP) consisting of [Au(BZI)(TMCz)]$^{+\cdot}$ and **1a**$^{-\cdot}$. We used nanosecond visible–near-infrared (Vis–NIR) transient absorption spectroscopy to

https://doi.org/10.1038/s41467-024-50979-6

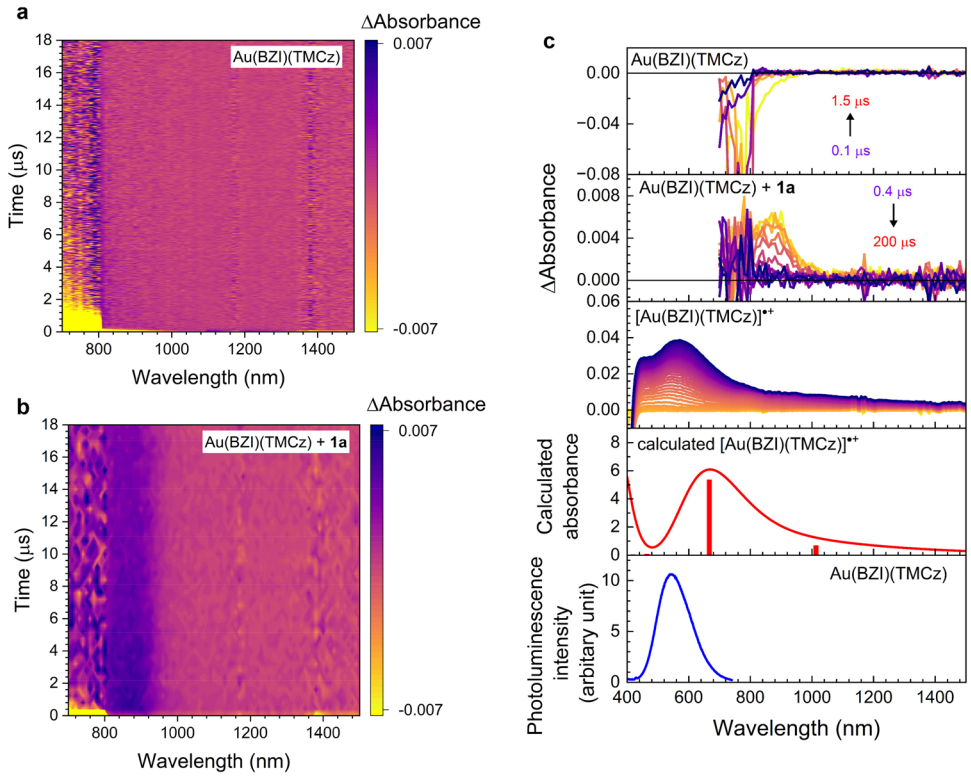

Fig. 5 | Electron transfer. a, **b** Heat maps showing nanosecond photoinduced transient Vis–NIR absorption difference signals of Ar-saturated DMSO containing 100 μM Au(BZI)(TMCz) recorded in the absence (**a**) and presence (**b**) of 200 mM **1a**, recorded after 355 nm pulsed laser photoexcitation. The legend shows ΔAbsorbance. **c** Top-most panel, selected photoinduced transient Vis–NIR absorption difference spectra of Ar-saturated DMSO containing 100 μM Au(BZI)(TMCz); second panel, selected photoinduced transient Vis–NIR absorption difference spectra of Ar-saturated DMSO containing 100 μM Au(BZI)(TMCz) recorded in the presence of 200 mM **1a**; third panel, Vis–NIR absorption difference spectra of 2.0 mM Au(BZI)(TMCz) recorded under an anodic potential of 0.45 V vs $Ag^{+/0}$ (conditions: Pt mesh working electrode, Pt coil counter electrode, $Ag/AgNO_3$ pseudo-reference electrode, and Ar-saturated DMSO containing 0.10 M Bu_4NPF_6 and the Au(I) complex); fourth panel, the absorption spectrum simulated for $[Au(BZI)(TMCz)]^{•+}$ (CAM-B3LYP and LANL2DZ basis sets for Au and 6–311+g(d,p) basis set for the other atoms), where the vertical bars indicate oscillator strengths; bottom-most panel, photoluminescence spectrum of Ar-saturated DMSO containing 10 μM Au(BZI)(TMCz).

directly monitor the genesis of the radical-ion species. As shown in Fig. 5a, the heat map of the photoinduced Vis–NIR absorption difference spectra of 100 μM Au(BZI)(TMCz) after nanosecond pulsed laser photoexcitation at a wavelength of 355 nm contains negative signals in the visible region because of the stimulated emission (see also the top- and bottom-most panels in Fig. 5c). In sharp contrast, positive signals emerge at a peak wavelength of 870 nm in the presence of 200 mM **1a** (Fig. 5b and the second panel in Fig. 5c). The NIR signals are attributable to $[Au(BZI)(TMCz)]^{•+}$ because $[Au(BZI)(TMCz)]^{•+}$ electrochemically generated at an anodic potential of 0.45 V vs $Ag^{+/0}$ exhibits a broad absorption band in this region (third panel in Fig. 5c). This spectral assignment is further corroborated by the close match with the $[Au(BZI)(TMCz)]^{•+}$ electronic transition spectrum quantum chemically simulated at the CAM-B3LYP level of theory with a conductor-like polarizable continuum model parameterized to DMSO (fourth panel in Fig. 5c). The transient spectroscopy and calculation investigations provide direct evidence for photoinduced electron transfer from $[Au(BZI)(TMCz)]^*$ to **1a**.

Once formed, the RIP is rapidly annihilated by charge recombination through back electron transfer from $\mathbf{1a}^{•-}$ to $[Au(BZI)(TMCz)]^{•+}$ because the driving force for charge recombination ($-\Delta G_{CR}$, $-\Delta G_{CR} = e\cdot[E_{red}(\mathbf{1a}) - E_{ox}(Au(BZI)(TMCz))]$) is as large as 2.37 eV. Notably, in many photoredox catalysis processes, the charge recombination is ultrafast and detrimental to the catalysis cycle, limiting the overall photocatalytic performance[36,39]. The charge recombination process in $[Au(BZI)(TMCz)]^{•+}$ can be monitored at a wavelength of 870 nm. Surprisingly, $[Au(BZI)(TMCz)]^{•+}$ is long-lived, with an apparent lifetime of 18 μs (Fig. 6a). Second-order kinetics analyses based on the molar absorbance of $[Au(BZI)(TMCz)]^{•+}$ at 870 nm (96 M^{-1} cm^{-1}) indicate that the rate constant for charge recombination (k_{CR}) with $\mathbf{1a}^{•-}$ is $3.3 \pm 0.1 \times 10^8$ M^{-1} s^{-1} (Fig. 6b). Notably, the yield for the liberation of free-radical-ion species from the geminate RIP (i.e., $[[Au(BZI)(TMCz)]^{•+}\cdot\cdot\cdot\mathbf{1a}^{•-}] \rightarrow [Au(BZI)(TMCz)]^{•+}$ and $\mathbf{1a}^{•-}$) can be computed according to the relationship k_{-diff} / ($k_{-diff} + k_{CR}$) to be as large as 91%. This value is greater than the yield for charge recombination of cyclometalated Pt(II) complexes with $CF_3I^{•-}$ (47–77%), which are highly reducing photocatalysts established by us[36]. The k_{CR} values with other aryl halide substrates were also determined to be in the range (0.7 ± 0.04 to 2.9 ± 0.7) $\times 10^9$ M^{-1} s^{-1} (Supplementary Fig. 7). Finally, we found that the k_{CR} values adhere to the Jortner curves for electron transfer with large reorganization energies, which suggested strong interactions with solvents (Supplementary Fig. 8).

The liberated $\mathbf{1a}^{•-}$ is cleaved into an aryl radical species and Cl^-. The aryl radical species subsequently reacts with **2a** to form a C–C cross-coupled adduct (**3aaH•** in Fig. 7). We hypothesized that the **3aaH•** species plays a key role in completing the photoredox catalytic cycle. Specifically, we hypothesized that the $[Au(BZI)(TMCz)]^{•+}$ is neutralized to the original Au(BZI)(TMCz) state through one-electron withdrawal from **3aaH•** and that DIPEA subsequently deprotonates the resultant one-electron-oxidized $\mathbf{3aaH}^+$ intermediate, producing the final product (**3aa**).

To validate this hypothesis, we performed nanosecond laser flash photolysis for the mixture of 100 μM Au(BZI)(TMCz) and 50 mM **1a** with the addition of **2a** in various concentrations (0–300 mM). We

https://doi.org/10.1038/s41467-024-50979-6

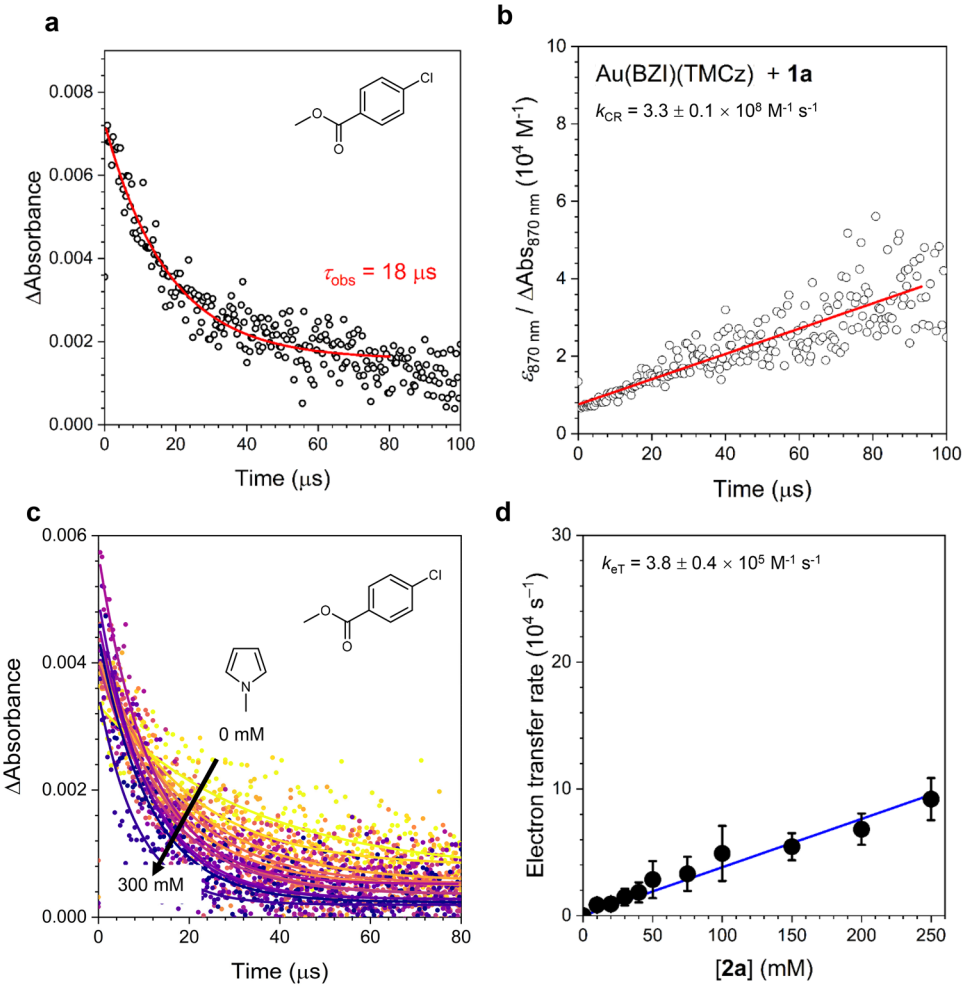

Fig. 6 | Electron transfer kinetics. a Temporal changes of the 870 nm [Au(BZI)(TMCz)]$^{•+}$ traces. **b** Second-order kinetics analysis for charge recombination between [Au(BZI)(TMCz)]$^{•+}$ and **1a**$^{•-}$. See Supplementary Fig. 7 for the results for the other substrates. **c** Decay traces recorded at 870 nm in the presence of 50 mM **1a** and increased concentrations of **2a** (0–300 mM). **d** Pseudo-first-order kinetics analysis for the catalyst recovery through electron transfer to [Au(BZI)(TMCz)]$^{•+}$. Error bars indicate the standard deviations of exponential fits of the data points in (**c**). See Supplementary Fig. 9 for the results for the other substrates.

expected that the effective concentration of **3aaH•** would increase with the increased **2a** concentration. Gratifyingly, we found that the increase in concentration of **2a** shortens the lifetime of the 870 nm signal of [Au(BZI)(TMCz)]$^{•+}$ (Fig. 6c). The concentration-dependent decays can be best interpreted as the recovery of Au(BZI)(TMCz) through electron transfer from **3aaH•** to [Au(BZI)(TMCz)]$^{•+}$. Our pseudo-first-order kinetics analysis of the 870 nm signals as a function of [**2a**] yields a second-order rate constant of $3.8 \pm 0.4 \times 10^5\,M^{-1}\,s^{-1}$ for bimolecular electron transfer (k_{eT}) from **3aaH•** to [Au(BZI)(TMCz)]$^{•+}$ (Fig. 6d). Results obtained with the other substrates are summarized in Supplementary Fig. 9. Although the determined value should serve as a lower limit due to the pre-steps for the generation of **3aaH•**, this k_{eT} value is three orders of magnitude smaller than the rate constants for the other electron-transfer steps, k_Q ($9.1 \pm 0.1 \times 10^8$ M^{-1} s^{-1}) and k_{CR} ($3.3 \pm 0.1 \times 10^8\,M^{-1}$ s^{-1}). This comparison indicates that the catalyst recovery is the rate-determining step in the overall photoredox catalysis cycle. The relatively slow electron transfer is presumably attributable to the multiple steps, including C–Cl bond cleavage and the radical addition to **2a**, required to form **3aaH•**.

Discussion

Given its enormous potential, photoredox catalysis will continue to expand our horizon of synthetic organic methodologies. This exploration inevitably requires the development of catalysts with strong redox power; it also requires kinetic compatibility of electronic processes involved in the catalytic cycle. In this research, we investigated the homogeneous photoredox catalysis of two-coordinated Au(I) complexes showing exclusive LLCT transition. Compared to organic TADF molecules exhibiting qualitatively similar intramolecular CT transition, the dipolar Au(I) complexes enable better utilization of photons for redox catalysis due to the Au(I) center. The advantages of Au(I) photoredox catalysts include (1) strong visible-light absorption, (2) cathodic E^*_{ox}s capable of reductively activating redox-resistant (hetero)aryl chloride substrates, (3) submicrosecond τ_{obs}, enabling efficient excited-state heterobimolecular processes, (4) effective suppression of charge recombination, and (5) versatility for controlling the E^*_{ox} and τ_{obs} values through ligand structures. We exploited these features to catalyze C–C cross-coupling reactions between (hetero)aryl halides, including (hetero)aryl chlorides, and *N*-heterocycles. Notably, our photoredox catalysis protocols require a minimal catalyst loading as low as 0.1 mol%. In addition, the catalysis exhibits a broad substrate scope.

Our mechanistic investigations revealed that the catalytic cycle of the C–C cross-coupling reaction is initiated by one-electron transfer from the excited-state Au complex to the aryl chloride substrate. Of particular interest is the long-lived (18 μs) radical-ion species because most photoredox catalysts suffer from rapid charge recombination before the subsequent catalysis step. Indeed, the yield for the radical

https://doi.org/10.1038/s41467-024-50979-6

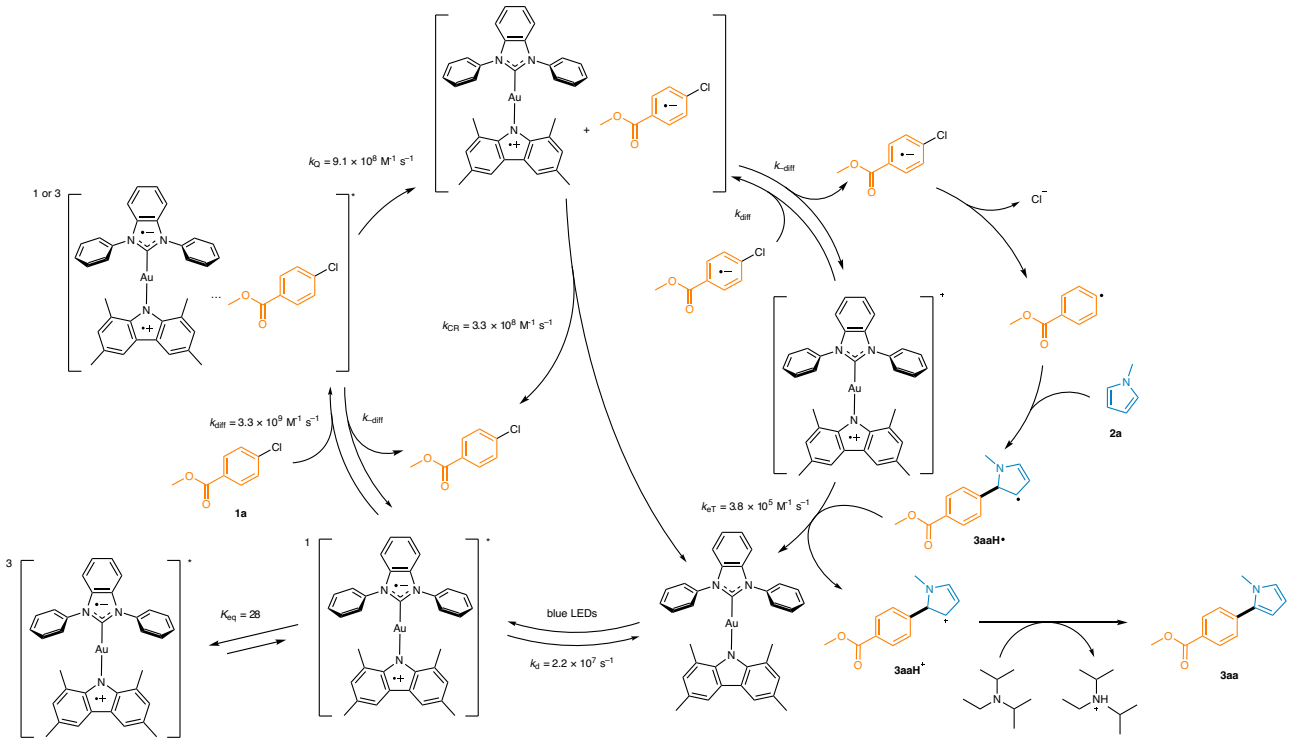

Fig. 7 | Catalysis cycle. Plausible mechanism of the photoredox catalytic C–C cross-coupling reaction. Refer to the main text for the definitions of the symbols.

intermediate is as large as 91%, validating the highly efficient production pathway. We also discovered that the final step (i.e., the recovery of the photocatalyst) is completed by electron transfer from the radical species of the C–C cross-coupled adduct and that the overall catalysis is governed by this step.

Our research provides photoredox catalytic organic transformation by LLCT-active Au(I) complexes. Mechanistic investigations also indicated electron-transfer behaviors beneficial for a range of photoredox catalytic applications, which will inspire future research toward developing organic synthesis methodologies that require strong photoreduction capability. One potential drawback of using Au(I) photoredox catalysts would be the irreversibility found in their cyclic voltammograms. Given the broad structural modularity of two-coordinate coinage metal complexes, we envision that the photoredox catalytic ability can be maximized upon judicious control over the metal center and the anionic and charge-neutral ligands.

Methods

Photoredox catalytic C(Ar)–C(Ar) cross-coupling reactions

An oven-dried reaction vial equipped with a magnetic stir bar was charged with (hetero)aryl halide **1** (0.50 mmol, 1.0 equiv), Au(BZI)(TMCz) (0.3 mg, 0.1 mol%), *N*-heterocycle **2** (5.0 mmol, 10 equiv), DIPEA (1.0 mmol, 2 equiv), and anhydrous DMSO (0.50 M, 1.0 mL). The vial was sealed with a silicon septum screw cap and purged with Ar via a balloon for 10 min. The vial was then exposed to blue LEDs (405 nm and 18 W) in a HepatoChem, P205-18-2 405 photoreactor with continuous stirring. The reaction vial was placed at 5 cm from the light source. The incident photon power density was determined to be 28 mW cm^{-2}. The reaction temperature was controlled using a chiller-heater unit. The emission spectrum and the instrumental setup are shown in Supplementary Fig. 10. The reaction progress was monitored using thin-layer chromatography (TLC) or gas chromatography (GC). Upon completion, the reaction was quenched by adding water. The reaction mixture was extracted three times using dichloromethane. The combined organic phases were dried over $MgSO_4$, concentrated under reduced pressure using a rotary evaporator, and purified by silica gel flash column chromatography using a hexane–ethyl acetate solution (10/1) as the eluent to give the corresponding C–C cross-coupled product **3**.

Steady-state UV–Vis absorption measurements

UV–Vis absorption spectra were collected on an Agilent, Cary 300 spectrophotometer at 298 K. Sample solutions were prepared prior to measurements at a concentration of 50 μM Au(BZI)(TMCz) dissolved in Ar-saturated DMSO and toluene, unless otherwise stated. The solution was delivered into a quartz cell (Hellma, beam path length = 1.0 cm).

Steady-state photoluminescence measurements

Photoluminescence spectra were obtained at 298 K using a Photon Technology International, Quanta Master 400 scanning spectrofluorometer. The solutions used for the steady-state UV–Vis absorption studies were also used for the photoluminescence measurements. The excitation wavelength for the solution of Au(BZI)(TMCz) was 380 nm unless otherwise stated. All the solutions were deaerated by bubbling Ar for 10 min prior to the measurements. A quartz cell (Hellma, beam path length = 1.0 cm) was used for solution samples.

Determination of photoluminescence lifetime

Photoluminescence decay traces were acquired on the basis of time-correlated single-photon counting (TCSPC) techniques, using a PicoQuant, FluoTime 200 instrument after 377 nm pulsed laser excitation (pulse duration = 25 ps). A picosecond pulsed diode laser that produced 377 nm (PicoQuant, LDH375) was driven by a PDL800-D driver (PicoQuant). Transient photon signals were collected at the peak emission wavelength for Au(BZI)(TMCz) through an automated motorized monochromator. The photon acquisition was terminated when the accumulated photon count reached 10^4. Photoluminescence decay traces were fitted to mono- or bi-exponential decay models embedded in the OriginLab, OriginPro 2022 software.

Determination of relative photoluminescence quantum yield

The photoluminescence quantum yield (Φ) was determined for 50 μM Au(BZI)(TMCz) dissolved in Ar-saturated DMSO and toluene. The Φ was calculated using the equation $\Phi = \Phi_{ref} \times (I/I_{ref}) \times (A_{ref}/A) \times (n/n_{ref})^2$, where A, I, and n are the absorbance at the excitation wavelength, the integrated photoluminescence intensity, and the refractive index of the solvent, respectively. 9,10-Diphenylanthracene ($\Phi_{ref} = 1.00$, toluene; $\lambda_{ex} = 366$ nm) was used as the reference material. Photoluminescence spectra were collected at 298 K in the emission range 400–740 nm and were integrated using the OriginLab, OriginPro 2022 software.

Photoluminescence quenching experiments

Photoluminescence spectra were obtained at 298 K using a Photon Technology International, Quanta Master 400 scanning spectrofluorometer. Stock solutions of 50 μM Au(BZI)(TMCz) and 500 mM and 5 M **1a** were prepared in DMSO. 3.0 mL of Au(BZI)(TMCz) solution was added into a quartz cell (Hellma, beam path length = 1.0 cm). Photoluminescence spectra of the Au(BZI)(TMCz) solution, which had been previously saturated with Ar, were taken ($\lambda_{ex} = 380$ nm) with the continuous addition of 3 μL of 500 μM and 5 mM **1a**. The final concentration of **1a** was 100 mM.

Electrochemical characterization

Cyclic and differential pulse voltammetry experiments were conducted using a CH Instruments, CHI630 B potentiostat with a three-electrode cell assembly. A Pt wire and a glassy carbon were used as the counter and working electrodes, respectively. An $Ag/AgNO_3$ couple was used as the pseudo-reference electrode. Measurements were carried out in Ar-saturated DMSO (3.0 mL) with 0.10 M NBu_4PF_6 as the supporting electrolyte at scan rates of 100 mV s^{-1} (cyclic voltammetry) and 4.0 mV s^{-1} (differential pulse voltammetry). A ferrocenium/ferrocene couple was employed as the external reference. The excited-state oxidation (E^*_{ox}) potentials were determined using the following relationship

$$E^*_{ox} = E_{ox} - \Delta E_g \quad (1)$$

In this equation, ΔE_g was determined from the onset wavelength of photoluminescence spectrum: 2.72 eV.

Determination of photochemical quantum yields (PCQYs)

The quantum yield for C–C cross-coupling was determined by conducting standard ferrioxalate actinometry. A 6 mM $K_3[Fe(C_2O_4)_3]$ solution as chemical actinometer was prepared, and 1 mL of solution was transferred to the same glassware used in the photoreaction (glass tube having a diameter of 1.5 cm), and the solution was photoirradiated with a beam of photoreaction at 405 nm for 20 s. The same volume of 1 wt% 1,10-phenanthroline in sodium acetate buffer solution was added and stored in the dark for 1 h. The absorbance changes at 510 nm were measured by UV–Vis spectrophotometer (Agilent, Cary 300); inserting the value to the following equation returned light intensities 8.31×10^9 einstein s^{-1} at 405 nm:

$$\text{light intensity}\,(I_0, \text{einstein}\,s^{-1}) = (\Delta\text{Abs}(510\,\text{nm}) \times V)/(\Phi \times 11050\,M^{-1}\,cm^{-1}\Delta t) \quad (2)$$

where, ΔAbs(510 nm), V, Φ, and Δt are the absorbance change at 510 nm, volume (L), quantum yield (1.15) of the ferrioxalate actinometer at 405 nm, and photoirradiation time (s), respectively. Finally, the reaction yield for C–C cross coupling with the reaction condition utilizing 0.1 mol% Au(BZI)(TMCz) as photoredox catalyst was quantified with GC-MS, and inserted into the following equation to afford PCQY:

$$\text{PCQY} = \frac{[\text{product}] \times V}{I_0 \times \triangle t} \quad (3)$$

where, [product] is the molar concentration of the products calculated from GC-MS, Δt (s) is the photoirradiated time, V is the volume of the solution (L), and I_0 is the light intensity obtained by actinometry described above.

Spectroelectrochemical measurements

UV–Vis–NIR absorption spectra of the radical species were obtained on an Agilent, Cary 5000 spectrophotometer by applying the anodic potentials (0.45 V vs $Ag/AgNO_3$) for Au(BZI)(TMCz), using the amperometric I–t curve method. A blank spectrum was taken for a 0.10 M NBu_4PF_6 solution (DMSO) in a spectroelectrochemical cell (path length = 0.5 mm) equipped with a Pt mesh working electrode, a Pt wire counter electrode, and an $Ag/AgNO_3$ pseudo-reference electrode. Then, 500 μL of a 2.0 mM sample solution was delivered into the spectroelectrochemical cell for the measurement.

Quantum chemical calculations

Geometry optimization was performed using Becke's three-parameter exchange-correlation functional (CAM-B3LYP), the double-ξ quality LANL2DZ basis set for the Au atom, and the 6–311+G(d) basis set for all the other atoms using the Gaussian 16, Revision B.01 program. A pseudo potential (LANL2DZ) was applied to replace the inner core electrons of the Au(I) atom, leaving the outer core electrons and the valence electrons. Time-dependent density functional theory (TD–DFT) calculations were carried out for the optimized geometries using the same functional and basis sets.

Nanosecond laser flash photolysis

Ar-saturated DMSO containing 100 μM Au(BZI)(TMCz) in a 1 × 1 cm quartz cell was excited by a Nd:YAG laser (Continuum, SLII-10; 355 nm and 5 mJ $pulse^{-1}$) in the absence and presence of 200 mM **1a**. Time courses of the transient absorption were measured using a photomultiplier tube (visible region) and an InGaAs-PIN photodiode (Hamamatsu 2949) (NIR region). The output from the photomultiplier tube and photodiode was recorded with a digitized oscilloscope (Tektronix, TDS3032; 300 MHz). All experiments were performed at 298 K. For titration experiments, stock solutions of 100 μM Au(BZI)(TMCz) and 1.11 M **2a** were prepared in DMSO. Au(BZI)(TMCz) solution (3.0 mL) was added to a 1 × 1 cm quartz cell. Decay traces of $[Au(BZI)(TMCz)]^{\bullet+}$ were recorded with the continuous addition of **2a**. The final concentration of **2a** was 300 mM.

Data availability

The datasets generated during and/or analyzed during the current study are available from the corresponding author on request. Coordinates of optimized structures are provided in the Source Data file. Source data are provided with this paper.

References

1. Romero, N. A. & Nicewicz, D. A. Organic photoredox catalysis. *Chem. Rev.* **116**, 10075–10166 (2016).
2. Prier, C. K., Rankic, D. A. & MacMillan, D. W. C. Visible light photoredox catalysis with transition metal complexes: applications in organic synthesis. *Chem. Rev.* **113**, 5322–5363 (2013).
3. Staveness, D., Bosque, I. & Stephenson, C. R. J. Free radical chemistry enabled by visible light-induced electron transfer. *Acc. Chem. Res.* **49**, 2295–2306 (2016).
4. Speckmeier, E., Fischer, T. G. & Zeitler, K. A toolbox approach to construct broadly applicable metal-free catalysts for photoredox

chemistry: deliberate tuning of redox potentials and importance of halogens in donor–acceptor cyanoarenes. *J. Am. Chem. Soc.* **140**, 15353–15365 (2018).
5. Arias-Rotondo, D. M. & McCusker, J. K. The photophysics of photoredox catalysis: a roadmap for catalyst design. *Chem. Soc. Rev.* **45**, 5803–5820 (2016).
6. Cybularczyk-Cecotka, M., Szczepanik, J. & Giedyk, M. Photocatalytic strategies for the activation of organic chlorides. *Nat. Catal.* **3**, 872–886 (2020).
7. Sajoto, T. et al. Blue and near-UV phosphorescence from iridium complexes with cyclometalated pyrazolyl or *N*-heterocyclic carbene ligands. *Inorg. Chem.* **44**, 7992–8003 (2005).
8. Hamze, R. et al. "Quick-silver" from a systematic study of highly luminescent, two-coordinate, d^{10} coinage metal complexes. *J. Am. Chem. Soc.* **141**, 8616–8626 (2019).
9. Ying, A. & Gong, S. A rising star: luminescent carbene-metal-amide complexes. *Chem. –Eur. J.* **29**, e202301885 (2023).
10. Bryden, M. A. & Zysman-Colman, E. Organic thermally activated delayed fluorescence (TADF) compounds used in photocatalysis. *Chem. Soc. Rev.* **50**, 7587–7680 (2021).
11. Kinoshita, T., Dy, J. T., Uchida, S., Kubo, T. & Segawa, H. Wideband dye-sensitized solar cells employing a phosphine-coordinated ruthenium sensitizer. *Nat. Photonics* **7**, 535–539 (2013).
12. Muniz, C. N., Schaab, J., Razgoniaev, A., Djurovich, P. I. & Thompson, M. E. π-Extended ligands in two-coordinate coinage metal complexes. *J. Am. Chem. Soc.* **144**, 17916–17928 (2022).
13. To, W.-P., Cheng, G., Tong, G. S. M., Zhou, D. & Che, C.-M. Recent advances in metal-TADF emitters and their application in organic light-emitting diodes. *Front. Chem.* **8**, 653 (2020).
14. Tang, R. et al. Au(I)-TADF emitters for high efficiency full-color vacuum-deposited OLEDs and TADF-sensitized fluorescent OLEDs with ultrahigh brightness and prolonged operational lifetime. *Adv. Opt. Mater.* **11**, 2300950 (2023).
15. Uoyama, H., Goushi, K., Shizu, K., Nomura, H. & Adachi, C. Highly efficient organic light-emitting diodes from delayed fluorescence. *Nature* **492**, 234–238 (2012).
16. Che, C.-M., Kwong, H.-L., Yam, V. W.-W. & Cho, K.-C. Spectroscopic properties and redox chemistry of the phosphorescent excited state of $[Au_2(dppm)_2]^{2+}$[dppm = bis(diphenylphosphino)methane]. *J. Chem. Soc. Chem. Commun*. 885–886 (1989).
17. Li, D., Che, C.-M., Kwong, H.-L. & Yam, V. W.-W. Photoinduced C–C bond formation from alkyl halides catalysed by luminescent dinuclear gold(I) and copper(I) complexes. *J. Chem. Soc. Dalton Trans.* **1992**, 3325–3329 (1992).
18. Sahoo, B., Hopkinson, M. N. & Glorius, F. Combining gold and photoredox catalysis: visible light-mediated oxy- and aminoarylation of alkenes. *J. Am. Chem. Soc.* **135**, 5505–5508 (2013).
19. Shu, X.-Z., Zhang, M., He, Y., Frei, H. & Dean Toste, F. Dual visible light photoredox and gold-catalyzed arylative ring expansion. *J. Am. Chem. Soc.* **136**, 5844–5847 (2014).
20. Huang, L., Rudolph, M., Rominger, F. & Hashmi, S. K. Photosensitizer-free visible-light-mediated gold-catalyzed 1,2-difunctionalization of alkynes. *Angew. Chem., Int. Ed.* **55**, 4808–4813 (2016).
21. Martynova, E. A. et al. Energy transfer (EnT) photocatalysis enabled by gold-N-heterocyclic carbene (NHC) complexes. *Chem. Sci.* **13**, 6852–6857 (2022).
22. Muniz, C. N. et al. Two-coordinate coinage metal complexes as solar photosensitizers. *J. Am. Chem. Soc.* **145**, 13846–13857 (2023).
23. Cambié, D., Bottecchia, C., Straathof, N. J. W., Hessel, V. & Noël, T. Applications of continuous-flow photochemistry in organic synthesis, material science, and water treatment. *Chem. Rev.* **116**, 10276–10341 (2016).
24. Ravelli, D., Protti, S. & Fagnoni, M. Carbon-carbon bond forming reactions via photogenerated intermediates. *Chem. Rev.* **116**, 9850–9913 (2016).
25. Xie, J., Jin, H. & Hashmi, A. S. K. The recent achievements of redox-neutral radical C-C cross-coupling enabled by visible-light. *Chem. Soc. Rev.* **46**, 5193–5203 (2017).
26. Wang, C.-S., Dixneuf, P. H. & Soulé, J.-F. Photoredox catalysis for building C-C bonds from $C(sp^2)$-H bonds. *Chem. Rev.* **118**, 7532–7585 (2018).
27. Kim, H. & Lee, C. Visible-light-induced photocatalytic reductive transformations of organohalides. *Angew. Chem., Int. Ed.***51**, 12303–12306 (2012).
28. Nguyen, J. D., D'Amato, E. M., Narayanam, J. M. R. & Stephenson, C. R. J. Engaging unactivated alkyl, alkenyl and aryl iodides in visible-light-mediated free radical reactions. *Nat. Chem.* **4**, 854–859 (2012).
29. Revol, G., McCallum, T., Morin, M., Gagosz, F. & Barriault, L. Photoredox transformations with dimeric gold complexes. *Angew. Chem., Int. Ed.* **52**, 13342–13345 (2013).
30. Ghosh, I., Ghosh, T., Bardagi, J. I. & König, B. Reduction of aryl halides by consecutive visible light-induced electron transfer processes. *Science* **346**, 725–728 (2014).
31. Fajardo, J. Jr. et al. Photoredox catalysis mediated by tungsten(0) arylisocyanides. *J. Am. Chem. Soc.* **143**, 19389–19398 (2021).
32. Sinha, N., Wegeberg, C., Häussinger, D., Prescimone, A. & Wenger, O. S. Photoredox-active Cr(0) luminophores featuring photophysical properties competitive with Ru(II) and Os(II) complexes. *Nat. Chem.* **15**, 1730–1736 (2023).
33. Chmiel, A. F., Williams, O. P., Chernowsky, C. P., Yeung, C. S. & Wickens, Z. K. Non-innocent radical ion intermediates in photoredox catalysis: parallel reduction modes enable coupling of diverse aryl chlorides. *J. Am. Chem. Soc.* **143**, 10882–10889 (2021).
34. Xu, J. et al. Unveiling extreme photoreduction potentials of donor–acceptor cyanoarenes to access aryl radicals from aryl chlorides. *J. Am. Chem. Soc.* **143**, 13266–13273 (2021).
35. Cowper, N. G. W., Chernowsky, C. P., Williams, O. P. & Wickens, Z. K. Potent reductants via electron-primed photoredox catalysis: unlocking aryl chlorides for radical coupling. *J. Am. Chem. Soc.* **142**, 2093–2099 (2020).
36. Choi, W. J. et al. Mechanisms and applications of cyclometalated Pt(II) complexes in photoredox catalytic trifluoromethylation. *Chem. Sci.* **6**, 1454–1464 (2015).
37. Kirgan, R. A., Sullivan, B. P. & Rillema, D. P. Photochemistry and photophysics of coordination compounds: rhenium. *Top. Curr. Chem.* **281**, 45–100 (2007).
38. Xiang, M., Xin, Z.-K., Chen, B., Tung, C.-H. & Wu, L.-Z. Exploring the reducing ability of organic dye (Acr^+-Mes) for fluorination and oxidation of benzylic $C(sp^3)$–H bonds under visible light irradiation. *Org. Lett.* **19**, 3009–3012 (2017).
39. Zou, C., Miers, J. B., Ballew, R. M., Dlott, D. D. & Schuster, G. B. Electron transfer and back electron transfer in photoexcited ion pairs: forward and back directions have different maximum rates. *J. Am. Chem. Soc.* **113**, 7823–7825 (1991).

Acknowledgements

This work was supported by Midcareer Research Programs (RS-2023-00208856 to Y.Y. and NRF-2020R1A2C2009636 to E.J.C.) through National Research Foundation grants funded by the Ministry of Science, Information, and Communication Technology (ICT) and Future Planning (MSIP), and by the Yonsei University Research Fund (2023-22-0132 to Y.Y.).

Author contributions

B.H.J. performed spectroscopic and quantum chemical investigations, analyzed the data, and wrote the manuscript. J.J. designed and

synthesized the substrates, evaluated the catalysis performance, and co-wrote the manuscript. S.L. designed and performed spectroscopic and electrochemical experiments, analyzed the data, and co-wrote the manuscript. E.J.C. supervised the work at Chung-Ang University and co-wrote the manuscript. Y.Y. coordinated all of the experiments and analyses and co-wrote the manuscript. All authors contributed to the discussion on the study and edited the manuscript.

Competing interests
The authors declare no competing interests.

Additional information
Supplementary information The online version contains supplementary material available at https://doi.org/10.1038/s41467-024-50979-6.

Correspondence and requests for materials should be addressed to Eun Jin Cho or Youngmin You.

Peer review information *Nature Communications* thanks Daniela Arias-Rotondo and the other anonymous reviewer(s) for their contribution to the peer review of this work. A peer review file is available.